Modeling neuronal bursting: singularity theory meets neurophysiology

Alessio Franci, Guillaume Drion, Rodolphe Sepulchre

Modeling neuronal bursting: singularity theory meets neurophysiology*

Alessio Franci[1,*], Guillaume Drion[2,3], & Rodolphe Sepulchre[1,2]
[1] INRIA Lille-Nord Europe, Orchestron project, 40 avenue Halley F 59650 Villeneuve d'Ascq, France
[2] Department of Electrical Engineering and Computer Science, University of Liege, Liege, Belgium
[3] Neurophysiology Unit, GIGA Neurosciences, University of Liege, Liege, Belgium
[*] Corresponding author. Email: alessio.franci@inria.fr

Abstract

Exploiting the specific structure of neuron conductance-based models, the paper investigates the mathematical modeling of neuronal bursting. The proposed approach combines singularity theory and geometric singular perturbations to unfold the geometry of multiple time-scales attractors in the neighborhood of high-codimension singularities. We detect a three-time scale bursting attractor in the universal unfolding of the winged cusp singularity and discuss the physiological relevance of the bifurcation and unfolding parameters in determining a physiological route into bursting, that is, the transition between tonic spiking and bursting. The results suggest generality and simplicity in the organizing role of the winged cusp singularity for the global dynamics of conductance based models.

1 Introduction

Bursting is an important signaling component of neurons, characterized by a periodic alternance of bursts and quiescent periods. Bursts are short but high-frequency trains of spikes, contrasting with the absence of spikes during the quiescent periods. Bursting activity has been recorded in many neurons, both in vitro and in vivo, and electrophysiological recordings show a great variety of bursting time traces. All neuronal bursters share nevertheless a sharp separation between three different time scales: a fast time-scale for the spike generation, a slow time-scale for the intraburst spike frequency, and an ultra slow time-scale for the inter burst frequency. Many neuronal models exhibit bursting in some parameter range and many bursting models have been analyzed through bifurcation theory but the exact mechanisms leading to neuronal bursting are still poorly understood, both mathematically and physiologically. In particular, modeling the route to burst, that is the physiological regulation mechanisms that modulate the firing activity of a given neuron from a regular pacemaking activity to a bursting activity, has remained elusive to date.

As an attempt to advance the mathematical understanding of neuronal bursting, the present paper exploits the particular structure of conductance based neuronal models to attack with a local analysis tool the global structure of multiple time-scales attractors. Rooted in the seminal work of Hodgkin and Huxley [1], conductance-based models are nonlinear RC circuits consisting of one capacitance (modeling the cell membrane) in parallel with possibly many voltage sources with voltage dependent conductance (each modeling a specific ionic current). The variables of the model are the membrane potential (V)

*This paper presents research results of the Belgian Network DYSCO (Dynamical Systems, Control, and Optimization), funded by the Interuniversity Attraction Poles Programme, initiated by the Belgian State, Science Policy Office. The scientific responsibility rests with its authors.

and the gating (activation and inactivation) variables that model the kinetics of each ion channel. The vast diversity of ion channels involved in a particular neuron type leads to high-dimensional models, but all conductance-based models share two central structural assumptions:

> *(i)* a classification of gating variables in three well separated time-scales (fast variables - in the range of the membrane potential time scale $\sim 1ms$; slow variables - 5 to 10 times slower; and ultra-slow variables - 10 to hundreds time slower), which roughly correspond to the three time scales of neuronal bursting.
>
> *(ii)* each voltage regulated gating variable x obeys the first-order monotone dynamics $\tau_x(V)\dot{x} = -x + x_\infty(V)$, which implies that, at steady state, every voltage regulated gating variable is an explicit monotone function of the membrane potential, that is, $x = x_\infty(V)$.

Our analysis of neuronal bursting rests on these two structural assumptions. Assumption *(i)* suggests a three-time scale singularly perturbed bursting model, whose singular limit provides the skeleton of the bursting attractor. Assumption *(ii)* implies that the equilibria of arbitrary conductance-based models are determined by Kirchoff's law (currents sum to zero in the circuit), which provides a single algebraic equation in the sole scalar variable V. This remarkable feature calls for singularity theory [2] to understand the equilibrium structure of the model.

The results of applying singularity theory to neuronal bursting modeling are threefold.

First, we show that the universal unfolding of the winged cusp singularity contains the skeleton for a minimal three-time scales bursting attractor. The algebraic expression of the unfolding defines the fast dynamics. Slow adaptation of the bifurcation parameter defines the slow dynamics. Ultra-slow adaptation of one (affine) unfolding parameter defines the ultra-slow dynamics. We prove the existence of a hyperbolic bursting attractor in this three-dimensional model under mild assumptions. The geometric skeleton of the attractor is provided by singularity theory, while the persistence of the attractor away from the singular limit is proven by singular perturbation theory. By construction, the obtained burster has the remarkable feature of persisting under sharp time-scale separation, a property that many previously published models of bursting lack. The proposed construction is general and suggests a seemingly novel method to unfold the geometry of high-dimensional attractors. This method is of potential interest beyond the study of neuronal bursting.

Second, the abstract model suggested by singularity theory is put in correspondence to a minimal three-time scale neuronal bursting model that has physiological interpretability as a mathematical reduction of higher-dimensional conductance based models. The proposed model is essentially the neuronal phase portrait recently studied in [3] augmented with a physiologically relevant ultra-slow adaptation variable. We show that this model faithfully reproduces quantitatively different types of bursting. Most importantly, we show that singularity theory suggests a natural route to burst in this model and that the essential regulatory parameters have a clear physiological interpretation.

Third, we provide an algorithmic procedure to trace the winged cusp singularity in arbitrary conductance-based models. The proposed algorithm identifies a winged cusp singularity for physiological parameter values in the presence of ionic currents that have long been recognized as the electrophysiological ingredients of a bursting neuron. The proposed algorithm can be considered as a straightforward extension of the algorithm recently proposed in [4], showing that the transcritical bifurcation that organizes the genesis of bursting in a conductance-based model is indeed part of the unfolding of a winged cusp. As an example, we trace a winged cusp singularity in the original Hodgkin-Huxley model and show that the inclusion of a calcium channel makes the detected winged cusp physiological.

The existence of three-time scale bursters in the abstract unfolding of a winged cusp is presented in Section 2. Section 3 focuses on a minimal reduced model of neuronal bursting and uses the insight of singularity theory to describe a physiological route to bursting in this

model. Section 4 shows how to trace a winged cusp singularity in arbitrary conductance based models. The technical details of mathematical proofs are presented in an appendix.

2 Universal unfolding and multi-time scale attractors

2.1 A primer on singularity theory

We introduce here some notation and terminology that will be used extensively in the paper. The interested reader is referred to the main results of Chapters I-IV in [2] for a comprehensive exposition of the singularity theory used in this paper.

Singularity theory studies scalar bifurcation problems of the form

$$g(x,\lambda)=0, \quad x,\lambda\in\mathbb{R}, \tag{1}$$

where g is a smooth function. The variable x denotes the state and λ is the bifurcation parameter. The set of pairs (x,λ) satisfying (1) is called the *bifurcation diagram. Singular points* satisfy $g(x^\star,\lambda^\star)=\frac{\partial g}{\partial x}(x^\star,\lambda^\star)=0$. Indeed, if $\frac{\partial g}{\partial x}(x^\star,\lambda^\star)\neq 0$, then the implicit function theorem applies and the bifurcation diagram is necessarily regular at $(x^\star,\lambda^\star)$.

Except for the fold $x^2\pm\lambda=0$, bifurcations are not generic, that is they do not persist under small perturbations. Singularity theory is a robust bifurcation theory: it aims at classifying all possible persistent bifurcation diagrams that can be obtained by small perturbations of a given bifurcation.

A *universal unfolding* of $g(x,\lambda)$ is a parametrized family of functions $G(x,\lambda;\alpha)$, where α lies in the unfolding parameter space $\mathbb{R}^k$, such that

1) $G(x,\lambda;0)=g(x,\lambda)$

2) Given any $p(x)$ and a small $\mu>0$, one can find an α near the origin such that the two bifurcation problems $G(x,\lambda;\alpha)=0$ and $g(x,\lambda)+\mu p(x)=0$ are qualitatively equivalent.

3) k is the minimum number of unfolding parameters needed to reproduce all perturbed bifurcation diagrams of $g(x,\lambda)$. k is called the codimension of $g(x,\lambda)$.

Unfolding parameters are not bifurcation parameters. Instead, they change the qualitative bifurcation diagram of the perturbed bifurcation problem $G(x,\lambda;\alpha)=0$. That is why λ is a distinguished parameter in the theory. Historically, this parameter was associated to a slow time, whose evolution lets the dynamics visit the bifurcation diagram in a quasi-steady state manner. It will play the same role in the present paper, where we only consider two singularities and their universal unfolding:
the codimension 1 hysteresis

$$g^s_{hy}(x,\lambda)=-x^3-\lambda, \tag{2}$$

whose universal unfolding is shown to be [2, Chapter IV]

$$G^s_{hy}(x,\lambda;\ \beta)=-x^3-\lambda+\beta x, \tag{3}$$

the codimension 3 winged cusp

$$g^s_{wcusp}(x,\lambda)=-x^3-\lambda^2, \tag{4}$$

whose universal unfolding is shown to be [2, Section III.8 and Chapter IV]

$$G^s_{wcusp}(x,\lambda;\ \alpha,\beta,\gamma)=-x^3-\lambda^2+\beta x-\gamma\lambda x-\alpha. \tag{5}$$

The universal unfolding of codimension$\geq$1 bifurcations contains some codimension 1 bifurcation. For instance, the universal unfolding of the winged cusp possesses hysteresis bifurcations on the unfolding parameter hypersurface defined by $\alpha\gamma^2+\beta=0$, $\alpha\leq 0$. Even though such bifurcation diagrams are not persistent, they define *transition varieties* that

separate equivalence classes of persistent bifurcation diagrams, hence, providing a complete classification of persistent bifurcation diagrams.

An unperturbed bifurcation problem assumes the suggestive role of *organizing center*: all the perturbed bifurcation diagrams are determined and organized by the unperturbed bifurcation diagram, which contains them in power. Via the inspection of local algebraic conditions at the singularity, an organizing center provides a semi-global description of all possible perturbed bifurcation diagrams.

2.2 The hysteresis singularity and spiking oscillations

The hysteresis singularity has a universal unfolding $-x^3-\lambda+\beta x$ with persistent bifurcation diagram plotted in Figure 1A for $\beta > 0$. We use this algebraic curve to generate the phase portrait in Fig. 1B of the two-time scale model

$$\begin{aligned} \dot{x} &= G^s_{hy}(x, \lambda + y;\ \beta) && \text{(6a)} \\ &= -x^3 + \beta x - \lambda - y \\ \dot{y} &= \varepsilon(x - y) && \text{(6b)} \end{aligned}$$

Because y is a slow variable, it acts as a slowly varying modulation of the bifurcation

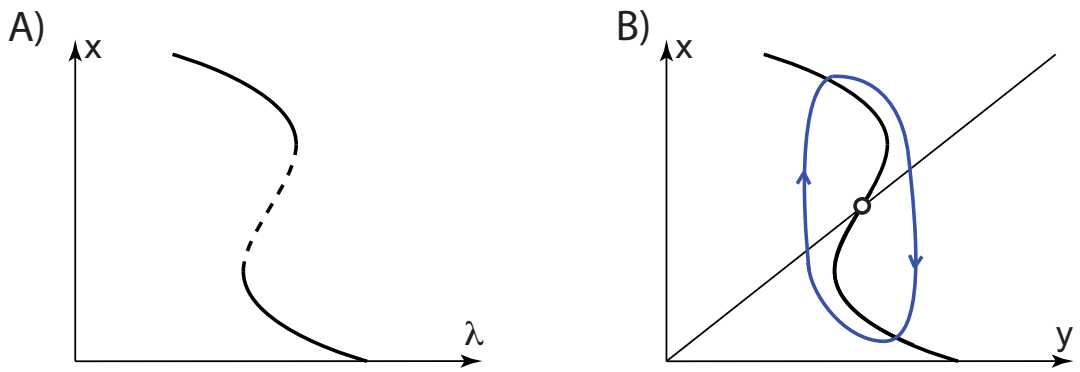

Figure 1: **Relaxation oscillations in the universal unfolding of the hysteresis bifurcation. A.** A persistent bifurcation diagram of the hysteresis singularity. Branches of stable (resp. unstable) fixed points are depicted as full (resp. dashed) lines. **B.** Through a slow adaptation of the bifurcation parameter, the bifurcation diagram in A. is transformed into the phase plane of a two-dimensional dynamical system, which still defines a universal unfolding of the hysteresis singularity. The thick full line is the fast subsystem nullcline. The thin full line is the slow subsystem nullcline. The circle denotes an unstable fixed point. For small $\beta > 0$, the model exhibits exponentially stable relaxation oscillations (depicted in light blue).

parameter in the fast dynamics (6a). As a consequence, the global analysis of system (6) reduces to a quasi-steady state bifurcation analysis of (6a), hence the relationship between Fig. 1A and Figure 1B.

The following theorem, proved in Section B.1, characterizes a well-known global attractor of (6).

Theorem 1 *For $\lambda = 0$ and for all $0 < \beta < 1$, there exists $\bar{\varepsilon} > 0$ such that, for all $\varepsilon \in (0, \bar{\varepsilon}]$, the dynamical system (6) possesses an exponentially stable relaxation limit cycle, which attracts all solutions except the equilibrium at $(0, 0)$.*

The familiar reader will recognize in (6) a famous model of neurodynamics introduced by FitzHugh [5]. It is the prototypical planar reduction of spiking oscillations. There is therefore a close relationship between the hysteresis singularity and spike generation.

2.3 The winged cusp singularity and rest-spike bistability

We repeat the elementary construction of Section 2.2 for the codimension-3 winged cusp singularity $-x^3 - \lambda^2$. It differs from the hysteresis singularity in the *non-monotonicity* of $g(x, \lambda)$ in the bifurcation parameter, that is $\frac{\partial(-x^3-\lambda^2)}{\partial\lambda} = -2\lambda$ changes sign at the singularity.

Figure 2A illustrates an important persistent bifurcation diagram in the unfolding of the winged cusp, obtained for $\gamma = 0$, $\beta > 0$, and $\alpha < -2\left(\frac{\beta}{3}\right)^{3/2}$. We call it the *mirrored hysteresis* bifurcation diagram. The right part ($\lambda > 0$) of this bifurcation diagram is essentially the persistent bifurcation diagram of the hysteresis singularity in Figure 1A. In that region, $\frac{\partial G^s_{wcusp}}{\partial\lambda} < 0$. The left part ($\lambda > 0$) is the mirror of the hysteresis and, in that region, $\frac{\partial G^s_{wcusp}}{\partial\lambda} > 0$. For $\gamma \neq 0$, the mirroring effect is not perfect, but the qualitative analysis does not change. The hysteresis and its mirror collide in a transcritical singularity for $\alpha = -2\left(\frac{\beta}{3}\right)^{3/2}$. This singularity belongs to the transcritical bifurcation transition variety in the winged cusp unfolding (see Appendix A). The transcritical bifurcation variety plays an important role in the forthcoming analysis.

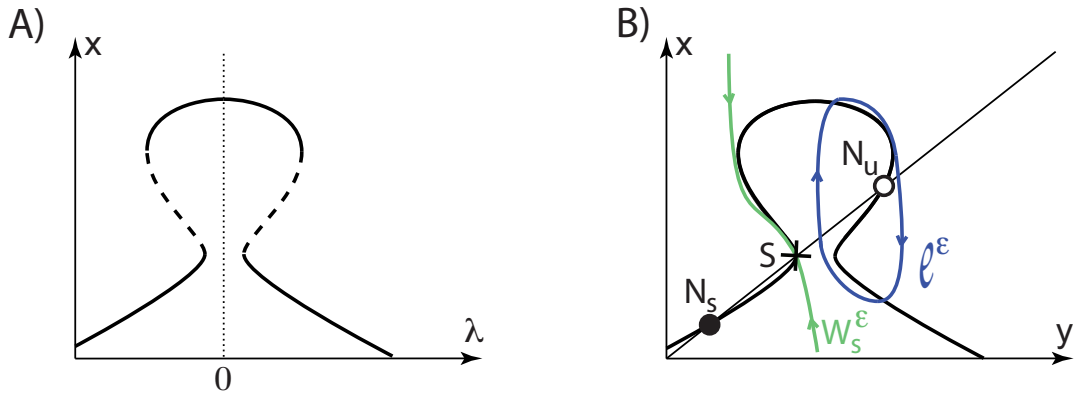

Figure 2: **Singularly perturbed rest-spike bistability in the universal unfolding of the winged cusp. A.** Persistent bifurcation diagram of the winged cusp for $\beta > 0$, $\alpha < -2\left(\frac{\beta}{3}\right)^{3/2}$, and $\gamma = 0$. **B.** A phase plane of (7).

We use the algebraic curve in Figure 2A to generate the phase portrait in Figure 2B of the two-dimensional model

$$\begin{aligned} \dot{x} &= G^s_{wcusp}(x, \lambda + y;\ \alpha, \beta, \gamma) && \text{(7a)} \\ &= -x^3 + \beta x - (\lambda + y)^2 - \gamma(\lambda + y)x - \alpha \\ \dot{y} &= \varepsilon(x - y). && \text{(7b)} \end{aligned}$$

Its fixed point equation

$$F(x, \lambda, \alpha, \beta, \gamma) := -x^3 + \beta x - (\lambda + x)^2 - \gamma(\lambda + x)x - \alpha. \qquad (8)$$

is easily shown to be again a universal unfolding of the winged cusp around $x_{wcusp} := \frac{1}{3}$, $\lambda_{wcusp} := 0$, $\alpha_{wcusp} := -\frac{1}{27}$, $\beta_{wcusp} := -\frac{1}{3}$, $\gamma_{wcusp} := -2$. The face portrait in Fig. 2B is a prototype phase portrait of rest-spike bistability: a stable fixed point coexists with a stable relaxation limit cycle.

Similarly to the previous section, the analysis of the singularly perturbed model (7) is completely characterized by the bifurcation diagram of Figure 2A. Such bifurcation

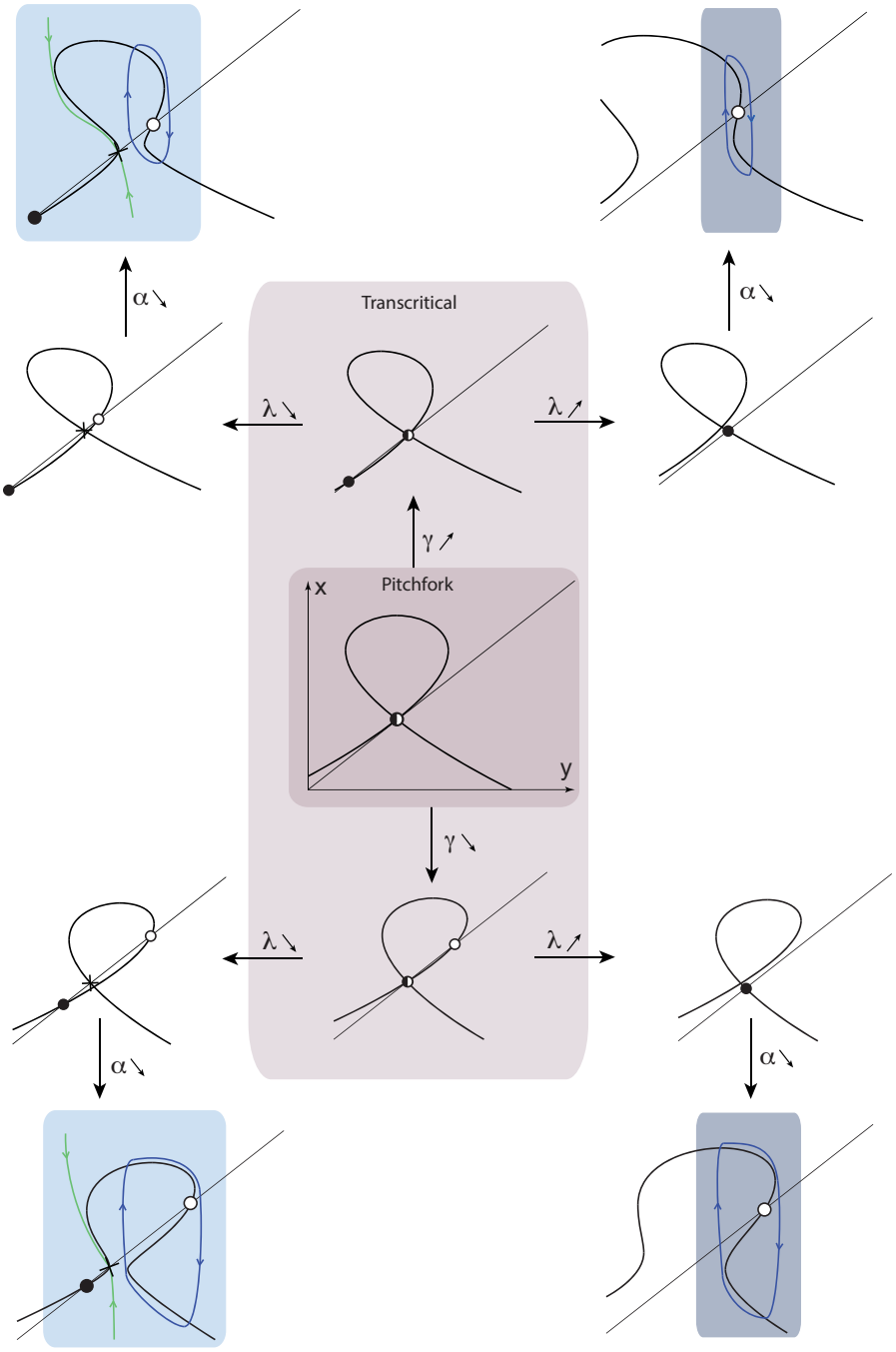

Figure 3: **An unfolding of the pitchfork bifurcation variety in (7).** The phase portraits in Figs. 1 and 2 both belong to the unfolding of the pitchfork singularity in center. A smooth deformation of the phase portrait of Fig. 1 into the phase portrait of Fig. 2 involves a transcritical bifurcation, which degenerate into a pitchfork for a particular value of the unfolding parameter γ

.

diagram provides a skeleton for the rest-spike bistable phase portrait in Figure 2B, as stated in the following theorem. Its proof is provided in Section B.2.

Theorem 2 *For all $\beta > \beta_{wcusp}$, there exist open sets of bifurcation (λ) and unfolding (α, γ) parameters near the pitchfork singularity at $(\lambda, \alpha, \gamma) = (\lambda_{PF}(\beta), \alpha_{PF}(\beta), \gamma_{PF}(\beta))$, in which, for sufficiently small $\varepsilon > 0$, model (7) exhibits the coexistence of an exponentially stable fixed point N_s and an exponentially stable spiking limit cycle ℓ^ε. Their basins of attraction are separated by the stable manifold W_s^ε of a hyperbolic saddle S* (see Fig. 2B).

Figure 3 shows the transition in (7) from the hysteresis phase portrait in Figure 1B to the bistable phase portrait in Fig. 2B through a transcritical bifurcation. Both phase portraits are generated by unfolding the degenerate portrait in Fig. 3, center, which belongs to the pitchfork bifurcation variety $(\alpha, \gamma) = (\alpha_{PF}(\beta), \gamma_{PF}(\beta))$, $\beta > \beta_{wcusp}$ (see Appendix A). The transcritical bifurcation variety $\alpha = \alpha_{TC}(\beta, \gamma)$ is obtained through variations of the unfolding parameter γ away from the pitchfork variety. It provides the two phase portraits in Fig. 3, center top and bottom. By increasing or decreasing the bifurcation parameter λ and decreasing the unfolding parameter α out of the transcritical bifurcation variety, these phase portraits perturb to the generic phase portraits in the corner, corresponding to the qualitative phase portraits in Figures 1B and Fig. 2B, respectively. The reader of [3] will recognize the same organizing role of the pitchfork in a planar model of neuronal excitability, see also Section 3.

2.4 A three-time scale bursting attractor in the winged cusp unfolding

The coexistence of a stable resting state and stable spiking oscillation, or *singularly perturbed rest-spike bistability*, makes (7) a good candidate as the slow-fast subsystem of a three-time scale minimal bursting model:

$$\begin{aligned} \dot{x} &= G^s_{wcusp}(x, \lambda + y;\ \alpha + z, \beta, \gamma) && \text{(9a)} \\ &= -x^3 + \beta x - (\lambda + y)^2 - \gamma(\lambda + y)x - \alpha - z \\ \dot{y} &= \varepsilon_1(x - y) && \text{(9b)} \\ \dot{z} &= \varepsilon_2 Z(x, y, z), && \text{(9c)} \end{aligned}$$

where $\varepsilon_1, \varepsilon_2 > 0$. The smooth function Z models the ultra-slow adaptation of the affine unfolding parameter α, in such a way that the global attractor of (9) will be determined by transition of (9a) through different persistent bifurcation diagrams.

The time scale separation between (9a-9b) and (9-c) makes it possible once again to derive a global analysis of model (9) from the analysis of the steady state behavior of (7) as α is varied. Such analysis can easily be derived geometrically in the singular limit $\varepsilon_1 = 0$. It is sketched in Figure 4. The different singular invariant sets in Figure 4A, can be glued together to construct the three-dimensional singular invariant set $\mathcal{M}_0$ in Figure 4B-left.

The singular invariant set $\mathcal{M}_0$ provides a skeleton for a three-time scale bursting attractor that shadows the branch $\mathcal{L}$ of stable fixed points in alternation with the branch P^0 of (singular) stable periodic orbits, as depicted in Figure 4B-right. To prove the existence of such an attractor, we only need to understand how $\mathcal{M}^0$ perturbs for $\varepsilon_1 > 0$.

Near the singular limit, the branch of singular periodic orbits P^0 perturbs to a nearby branch of exponentially stable periodic orbits P^ε (see Fig. 5), whereas the singular homoclinic trajectory SH^0 perturbs to an unstable homoclinic trajectory SH^ϵ (at $\alpha = \alpha^\epsilon_{SH}$). The branch of unstable periodic orbits Q^ε generated at SH^ε eventually merges with P^ε at a fold limit cycle bifurcation $\mathcal{F}_{LC}$ for some $\alpha^\varepsilon_{FLC} \in (\alpha^\epsilon_{SH}, \alpha^0_{SH})$. In the whole range $(\alpha_{SN}, \alpha^\varepsilon_{FLC})$, model (7) exhibits the coexistence of a stable fixed point and a stable spiking limit cycle. The details of this analysis are contained in Lemma 3 in Section B.3.

We follow [6, 7] to derive conditions on the bifurcation and unfolding parameters in (9a-9b) and choose a suitable Z in the ultra-slow dynamics (9c) such that z can hysteretically modulate the slow-fast subsystem (9a-9b) across its bistable range $(\alpha_{SN}, \alpha^\varepsilon_{FLC})$ to obtain stable bursting oscillations. The existence of such bursting oscillations is stated in the following theorem. Its proof is provided in Section B.3.

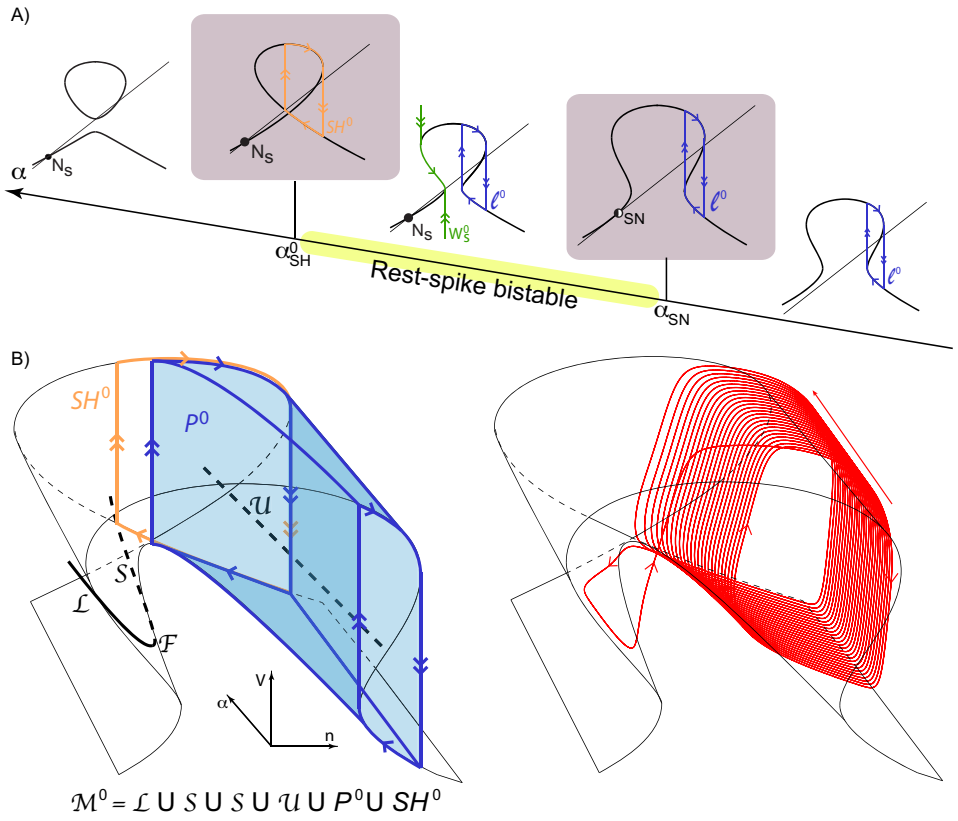

Figure 4: **Singular steady-state behavior of (7) through a variation of the unfolding parameter α. A.** Singular phase portraits of (7) for $\gamma = 0$, $\beta = \frac{1}{3}$, and small negative λ. For $\alpha \in (\alpha_{SN}, \alpha^0_{SH})$, the singularly perturbed model (7) exhibits rest-spike bistability, that is, the coexistence of a stable node N_s, a singular stable periodic orbit ℓ^0, and a singular saddle separatrix W^0_s. At $\alpha = \alpha^0_{SH} = -2\left(\frac{\beta}{3}\right)^{3/2}$ the left and right branches of the mirrored hysteresis bifurcation collide in a transcritical singularity that serves as a connecting point for a singular homoclinic trajectory SH^0. For $\alpha > \alpha^0_{SH}$, the only (singular) attractor is the stable node N_s. At $\alpha = \alpha_{SN}$, the saddle and the stable node merge in a saddle-node bifurcation SN. For $\alpha < \alpha_{SN}$, the only attractor is the singular periodic orbit ℓ^0. **B.** Gluing the different invariant sets in **A** leads to the three-dimensional singular invariant set $\mathcal{M}^0$ (left), which provides a skeleton for a three-time scale bursting attractor (right) in the singularly perturbed system (9). The branch of stable fixed points (resp. saddle point) for $\alpha < \alpha_{SN}$ is drawn as the black solid curve $\mathcal{L}$ (resp. the black dashed curve $\mathcal{S}$). The saddle node bifurcation connecting them is denoted by $\mathcal{F}$. The branch of unstable fixed points is drawn as the black dashed line $\mathcal{U}$. The branch of stable singular periodic orbit for $\alpha < \alpha^0_{SH}$ is drawn as the blue cilindric surface P^0. The singular saddle homoclinic trajectory is drawn as the orange oriented curve SH^0.

Theorem 3 *For all $\beta > \beta_{wcusp}$, there exists an open set of bifurcation (λ) and unfolding (α, γ) parameters near the pitchfork singularity at $(\lambda, \alpha, \gamma) = (\lambda_{PF}(\beta), \alpha_{PF}(\beta), \gamma_{PF}(\beta))$, in which, for sufficiently small $\varepsilon_1 \gg \varepsilon_2 > 0$ and suitable Z, model (9) has an hyperbolic bursting attractor.*

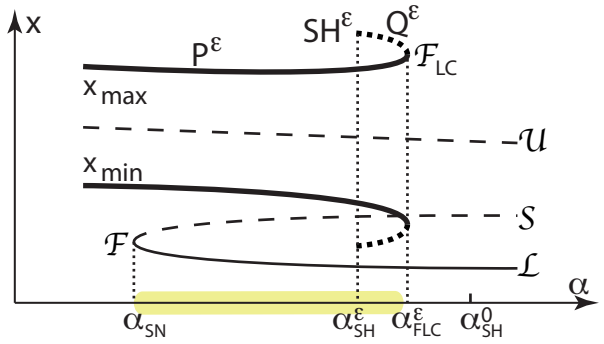

Figure 5: **Bifurcation diagram of (7) with respect the unfolding parameter α for sufficiently small ε.** The branch of stable fixed point is depicted as the full thin line $\mathcal{L}$, the branch of saddle point as the dashed thin line $\mathcal{S}$, and the branch of unstable fixed point as the dashed thin line $\mathcal{U}$. The branch of stable periodic orbit is depicted by the thick full lines P^ε and the branch of unstable periodic orbits by the thick dashed lines Q^ε. SH^ε: saddle-homoclinic bifurcation. $\mathcal{F}_{LC}$: fold limit cicle bifurcation. $\mathcal{F}$: fold (saddle-node) bifurcation. The yellow strip between the saddle-node and fold limit cicle bifurcation denotes the rest-spike bistable range.

3 Singularity theory provides a physiological route to neuronal bursting

3.1 A minimal three-time scale bursting model

The recent paper [3] introduces the planar neuron model

$$\dot{V} = V - \frac{V^3}{3} - n^2 + I \tag{10a}$$

$$\dot{n} = \varepsilon(n_\infty(V - V_0) + n_0 - n) \tag{10b}$$

Its phase portrait was shown to contain the pitchfork of Figure 3 as an organizing center, leading to distinct types of excitability for distinct values of the unfolding parameters. The analysis of the previous section suggests that a bursting model is naturally obtained by augmenting the planar model (10) with ultra slow adaptation:

$$\dot{V} = kV - \frac{V^3}{3} - (n + n_0)^2 + I - z \tag{11a}$$

$$\dot{n} = \varepsilon_n(V)\,(n_\infty(V - V_0) - n) \tag{11b}$$

$$\dot{z} = \varepsilon_z(V)(z_\infty(V - V_1) - z) \tag{11c}$$

Model (10) is essentially model (11) for $k = 1$ and $z = 0$, modulo a translation $n \leftarrow n+n_0$. The dynamics (11b-11c) mimic the kinetics of gating variables in conductance-based models, where the steady-state characteristics $n_\infty(\cdot)$ and $z_\infty(\cdot)$ are monotone increasing (typically sigmoidal) and the time scaling $\varepsilon_n(\cdot)$ and $\varepsilon_z(\cdot)$ are Gaussian-like strictly positive functions.

Details of model (11) for the numerical simulations of the paper are provided in Appendix C, but the assumption above are sufficient to prove (through tedious calculations not shown) that the model contains the same singularities as the abstract model (9) taking n_0 as the bifurcation parameter and (I, k, V_0) as unfolding parameters.

The difference between (11) and (9) is that the model (11) has the physiological interpretation of a reduced conductance-based model, with V a fast variable that aggregates

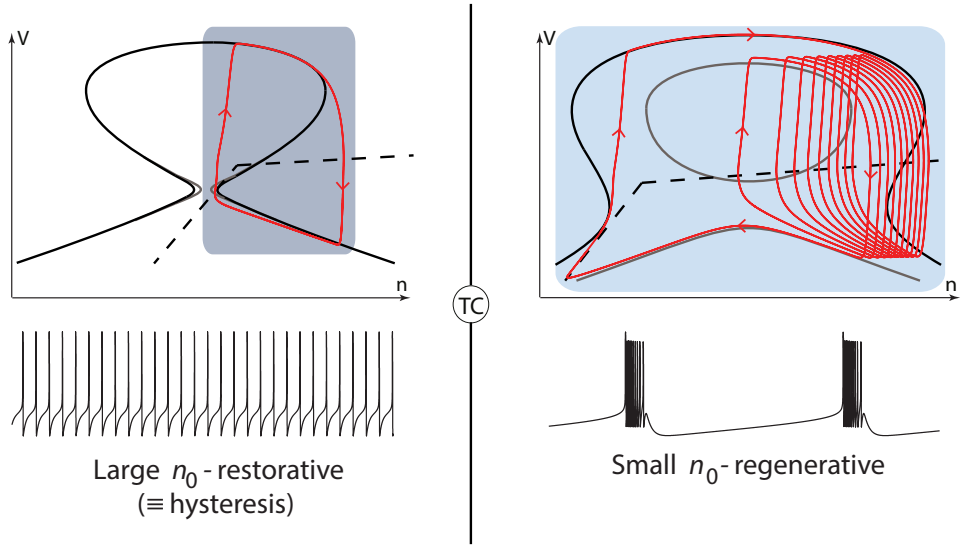

Figure 6: **Transition from restorative excitability (tonic firing) to regenerative excitability (bursting) in model (11) by sole variation of the bifurcation parameter n_0.** The analytical expression of the steady state functions $n_\infty(\cdot)$ and $z_\infty(\cdot)$ and numerical parameter values are provided in Appendix C. The time scale is the same in the left and right temoral traces.

the membrane potential with all fast gating variables, n a slow recovery variable that aggregates all the slow gating variables regulating neuronal excitability, and z an ultra-slow adaptation variable that aggregates the ultra-slow gating variables that modulate the cellular rhythm over the course of many action potentials. Finally, I models an external applied current.

3.2 Model parameters and their physiological interpretation

The bifurcation parameter n_0 models the balance between restorative and regenerative ion channels

The central role of the bifurcation parameter n_0 in (11) was analyzed in [3, 4] and is illustrated in Fig. 6. The transcritical bifurcation variety in Fig. 3 corresponds to the physiologically relevant transition from restorative excitability (large n_0) to regenerative excitability (small n_0). When the excitability is restorative, the recovery variable n provides negative feedback on membrane potential variations near the resting equilibrium, a physiological situation well captured by FitzHugh-Nagumo model (or the hysteresis singularity). In contrast, when excitability is regenerative, the recovery variable n provides positive feedback on membrane potential variations near the resting potential, a physiological situation that requires the quadratic term in (11a) (or the winged cusp singularity).

The value of n_0 in a conductance-based model reflects the balance between restorative and regenerative ion channels that regulate neuronal excitability. How to determine the balance in an arbitrary conductance-based model is discussed in [4]. Note that the restorative or regenerative nature of a particular ion channel in the slow time-scale is an intrinsic property of the channel. A prominent example of restorative channel is the slow potassium activation shared by (almost) all spiking neurons. A prominent example of regenerative channel is the slow calcium activation encountered in most bursting neurons. The presence of regenerative channels in neuronal bursters is well established in neurophysiology. See e.g. [8, 9].

The affine unfolding parameter provides bursting by ultra-slow modulation of the current across the membrane

For small n_0, the modulation of the ultra-slow variable z creates a hyperbolic bursting attractor through the hysteretic loop described in Fig. 4. The burster becomes a single-spike limit cycle (tonic firing) for large n_0 (restorative excitability), that is, in the absence of rest-spike bistability in the planar model.

The presence of ultra-slow currents in neuronal bursters is well established in neurophysiology (see e.g. [9]). A prominent example is provided by ultra-slow calcium activated potassium channels.

Half activation potential affects the route to bursting

The role of the unfolding parameter γ in (9) is illustrated in Fig. 3: it provides two qualitatively distinct paths connecting the restorative and regenerative phase portraits. This role is played by the parameter V_0 in the planar model (10) studied in [3], which has the physiological interpretation of a half activation potential. The role of half-activation potentials in neuronal excitability is well documented in neurophysiology (see e.g. [10]). The role of this unfolding parameter in the route to bursting is discussed in the next subsection.

No spike without fast autocatalytic feedback

The role of the unfolding parameter k in (11) is to provide positive (autocatalytic) feedback in the fast dynamics. The prominent source of this feedback in conductance-based models is the fast sodium activation. It is well acknowledged in neurodynamics [11].

Although not further elaborated in the present manuscript, the reduced model (11) makes clear predictions about its dynamical behavior in the absence of this feedback (*i.e.* $k = 0$). Those predictions are in closed agreement with the experimental observation of "small oscillatory potentials" when sodium channels are made silent with pharmacological blockers [12, 13].

3.3 A physiological route to bursting

A central insight of the reduced model (11) is that it provides a route to bursting: fixing all unfolding parameters and varying only the bifurcation parameter n_0 leads to a smooth transition from tonic firing to bursting, see Fig. 7. Smooth and reversible transitions

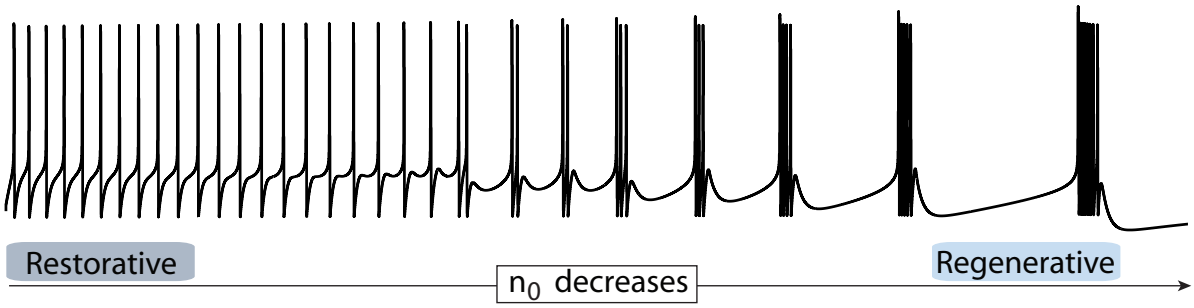

Figure 7: **Route from tonic firing to bursting in model (11) via a smooth variation of the bifurcation parameter n_0.** Rest of the parameter as in Figure 6.

between those two rhythms have been observed in many experimental recordings [14, 15], making the route to burst an important signaling mechanism. The fact that the modulation is achieved simply through the bifurcation parameter n_0, *i.e.* the balance between

restorative and regenerative channels, is of physiological importance because it is consistent with the physiology of experimental observations of routes into bursting.

The analysis in the above sections shows that the transition from single spike to bursting is through the transcritical bifurcation variety in model (7). Looking at the singular limit $\varepsilon = 0$ of (7) near this transition variety provides further insight on the geometry of the route that leads to the appearance of the saddle-homoclinic bifurcation organizing the bistable phase-portrait. This route is organized by the path through the pitchfork bifurcation, which provides the most symmetric path across the transcritical variety. The generic transitions are understood by perturbing the degenerate path.

Fig. 8A shows the qualitative projection of those paths onto the (V_0, n_0) parameter chart obtained in model (10) for $I = \frac{2}{3}$. The chart is reproduced from [3]. The same qualitative picture is obtained for the (γ, λ) parameter chart of the abstract model (7) at $\alpha = \alpha_{TC}(\beta, \gamma)$ (see Appendix A). The chart associates different excitability types (as well as their restorative or regenerative nature, see [4]) to distinct bifurcation mechanisms. Unfolding those paths along the I (or α) direction leads to the bifurcation diagrams in Fig. 9B. They reveal (in the singular limit) the onset of the bistable range organized by the singular saddle-homoclinic loop SH^0 as paths cross the transcritical bifurcation variety.

The same qualitative picture persists for $\varepsilon > 0$. Fig. 9 illustrates how the appearance of the singular saddle-homoclinic loop is accompanied, for $\varepsilon > 0$, by a smooth transition from a monostable (SNIC - route *i)*) or barely bistable (sub. Hopf - route *ii)*) bifurcation diagram to the robustly bistable bifurcation diagram constructed in the sections above (Fig. 5). Through ultra-slow modulation of the unfolding parameter α, this transition geometrically captures the transition from tonic spiking to bursting via the sole variation of the bifurcation parameter.

4 Tracing the winged cusp singularity in arbitrary conductance-based models

The winged cusp singularity emerges as an organizing center of rhythmicity in the reduced neuronal model (11), but a legitimate question is whether this singularity can be traced in arbitrary (high-dimensional) conductance-based models or is an artifact of the proposed reduction. Our recent paper [4] addresses a closely related question for the transcritical variety. It provides an analog of the bifurcation parameter n_0 in arbitrary conductance-based models of the form

$$C_m \dot{V} = -\sum_i \bar{g}_i m_i^{a_i} h_i^{b_i} (V - E_i) + I_{app}, \tag{12a}$$

$$\tau_{x^f}(V)\dot{x}^f = -x^f + x^f_\infty(V), \tag{12b}$$

$$\tau_{x^s}(V)\dot{x}^s = -x^s + x^s_\infty(V), \tag{12c}$$

$$\tau_{x^a}(V)\dot{x}^a = -x^a + x^a_\infty(V), \tag{12d}$$

where i spans all ionic currents, x^f spans all fast gating variables, x^s spans all slow gating variables, and x^a spans all ultra-slow (adaptation) variables (see [4] for more details on the adopted notation). A defining condition of the winged cusp singularity is the non-monotonicity of the quantity $\frac{\partial G_{wcusp}}{\partial \lambda}$, which implies the existence of a transcritical transition variety where $\frac{\partial G_{wcusp}}{\partial \lambda} = 0$. In arbitrary conductance-based models, this algebraic condition translates into a balance equation

$$\sum_{x^s} \frac{\partial \dot{V}}{\partial x^s} \frac{\partial x^s_\infty}{\partial V} = 0.$$

that expresses a perfect balance between the positive feedback of slow regenerative currents and the negative feedback of slow restorative currents.

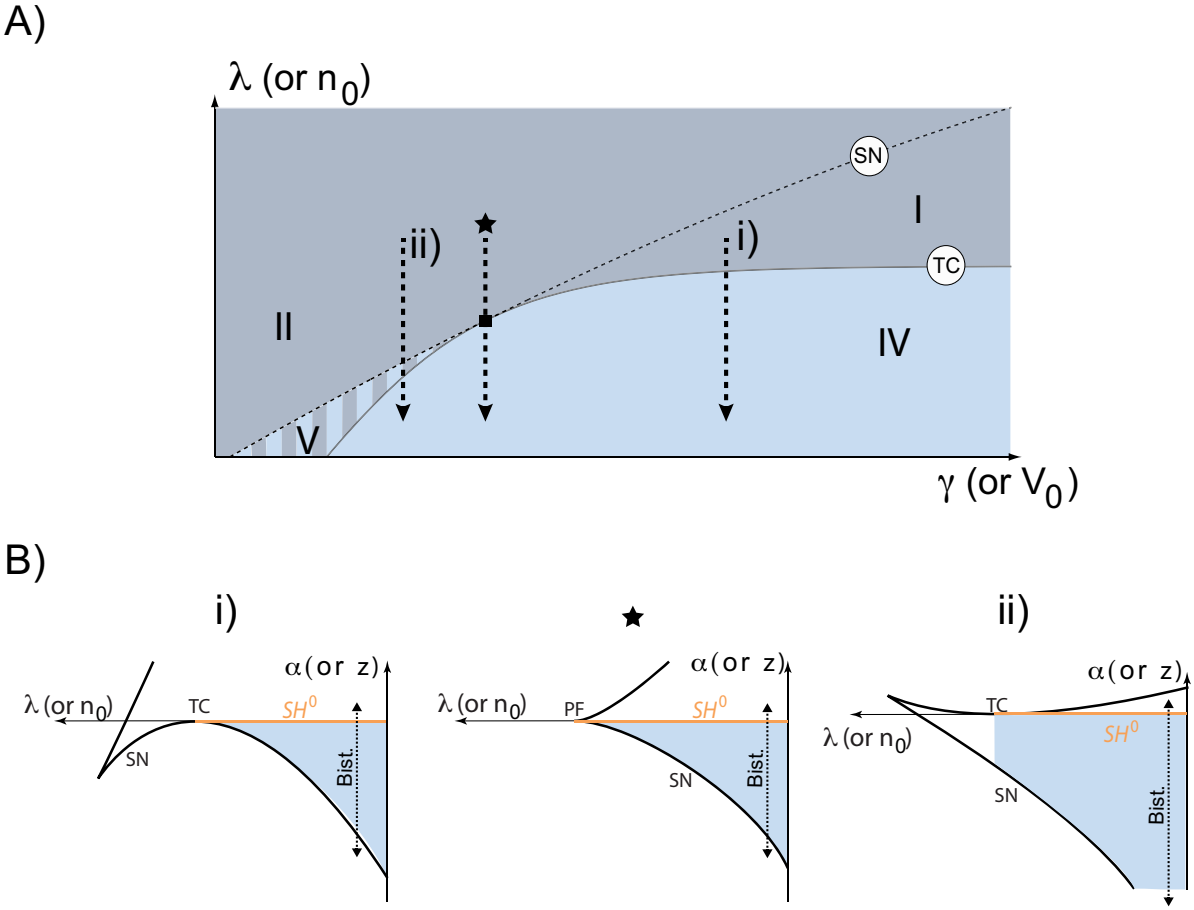

Figure 8: **Routes into bursting in the universal unfolding of the pithfork bifurcation. A.** Qualitative projection of routes into bursting onto the (V_0, n_0) (resp. (γ, λ)) of model (10) (resp. (7)) for $I = \frac{2}{3}$ (resp. $\alpha = \alpha_{TC}(\beta, \gamma)$, see Appendix A). Excitability is restorative in subregions I and II, mixed in subregion V, and regenerative in subregion IV. See [3] and [4] for details concerning the underlying bifurcation mechanisms. The transition path labeled with a star depicts the degenerate path across the pitchfork. The generic paths *i)* and *ii)* are distinguished by different half activation potentials V_0 (resp. unfolding parameter γ). **B.** Unfolding of transition paths in A along the I (resp. α) direction. Black thick lines denote branches of saddle-node (SN) bifurcation. In paths *i)* and *ii)*, the model undergoes a transcritical bifurcation (TC) as the path touches tangentially a branch of SN bifurcations. In the degenerate path, the model undergoes a pitchfork (PF) bifurcation as the path enters the cusp tangentially to both branches of SN bifurcations. The singular saddle-homoclinic loop, geometrically constructed in Figs. 4 and 9, is denoted by SH^0 and determines the appearance of a singular bistable range persisting away from singular limit.

We use the insight of [4] to trace a winged cusp in arbitrary conductance-based models, which indirectly establishes that the transcritical bifurcations and the associated excitability switches described in [4] are always in the universal unfolding of a winged cusp.

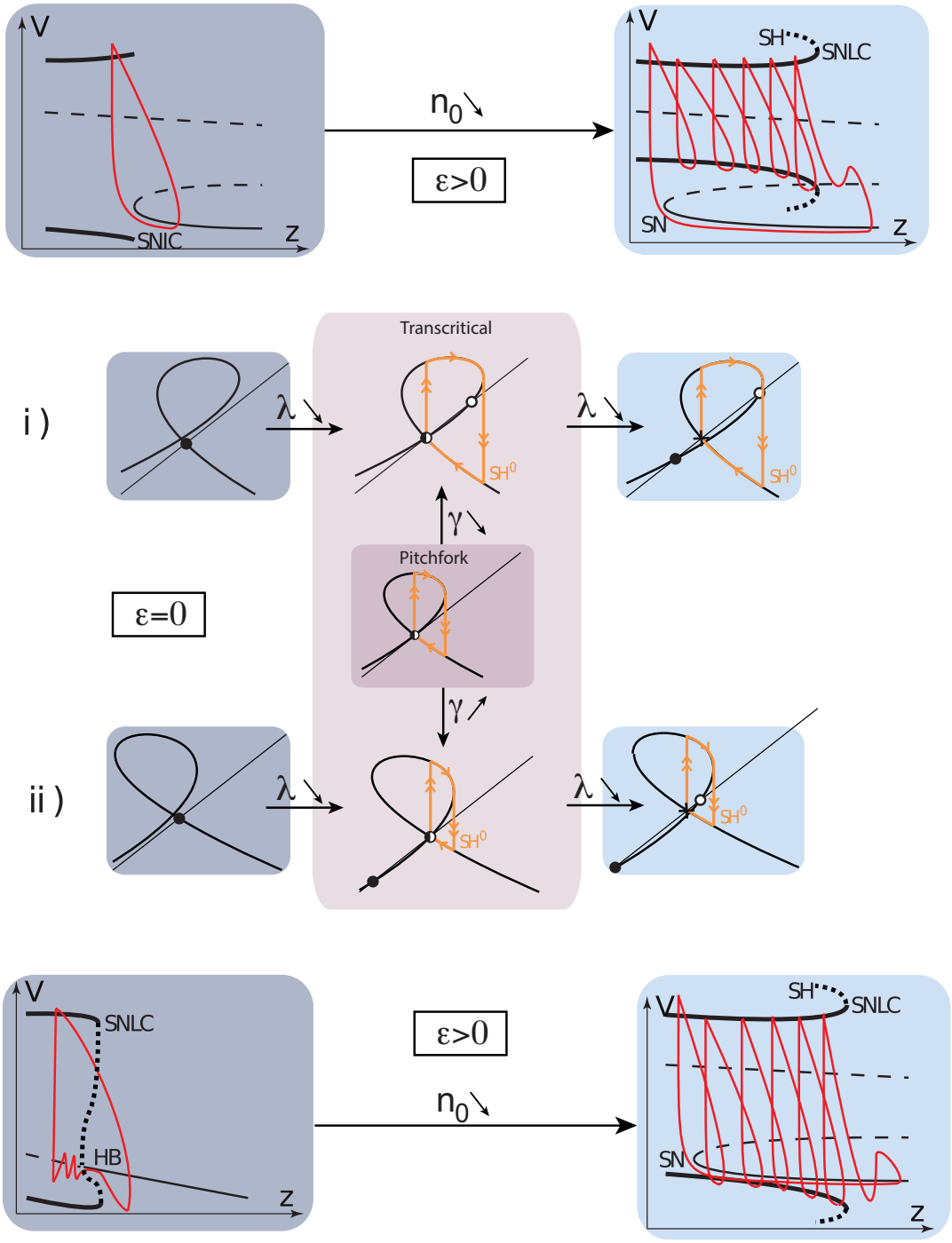

Figure 9: **Geometry of the two generic routes into bursting in the unfolding of the pitchfork bifurcation in model (9) and model (11).**

4.1 A winged cusp universal unfolding in the Hodgkin-Huxley model

The first conductance-based model appears in the seminal paper of Hodgkin-Huxley [1]

$$
\begin{aligned}
C\dot{V} &= -\bar{g}_K n^4 (V - V_K) - \bar{g}_{Na} m^3 h (V - V_{Na}) - g_l (V - V_l) + I \\
\tau_m(V)\dot{m} &= -m + m_\infty(V) \\
\tau_n(V)\dot{n} &= -n + n_\infty(V - V_{1/2,K}) \\
\tau_h(V)\dot{h} &= -h + h_\infty(V),
\end{aligned}
$$

where the time constants τ_x the steady state characteristics x_∞, $x = m, n, h$, and the potassium half-activation $V_{1/2,K}$ are chosen in accordance with the original model (see Appendix D). The model only accounts for two ionic currents: sodium, with its fast activation variable m and slow inactivation h, and potassium, with slow activation n. The classical phase portrait reduction [5, 16] is obtained with the quasi-steady state approximation $m \simeq m_\infty(V)$ and the empirical fit $h \simeq 1 - n$. It is well known that in its physiological part ($0 < n < 1$) this phase portrait is qualitatively the FitzHugh phase portrait in Fig. 1. But we showed in [17] (Figure 5) that the entire phase portrait ($n \in \mathbb{R}$) indeed also contains the "mirrored" phase portrait of Fig. 2. This observation suggests that a winged cusp organizes Hodkgin-Huxley dynamics. The singularity is found in a non-physiological range of the phase space ($n < 0$), which is consistent with the absence of slow regenerative currents in the model.

Because a negative value of n is non physiological, we expect a "non-physiological" winged cusp organizing Hodgkin-Huxley dynamics, which is consistent with the absence of slow regenerative currents in this model. Following [4] the balance equation reads

$$\frac{\partial \dot{V}}{\partial n}\frac{\partial n_\infty}{\partial V} + \frac{\partial \dot{V}}{\partial h}\frac{\partial h_\infty}{\partial V} = 0, \tag{13a}$$

which can be satisfied only for a negative value of the maximal conductance $\bar{g}_K$ in the (physiological) voltage range $V_K < V < V_{Na}$. Picking $\bar{g}_K$ as the bifurcation parameter and $(I, V_{1/2,K}, \bar{g}_{Na})$ as unfolding parameters, we indeed find a winged cusp singularity around $V \simeq -40mV$ and $\bar{g}_K \simeq -3\ 10^{12} mS/cm^2$. Since, by direct numerical inspection, the non-degeneracy condition [2, eq. III.4.20] is satisfied, [2, Proposition III.4.5] also implies that with the chosen unfolding parameters the Hodgkin-Huxley dynamics lives in the universal unfolding of the winged cusp: despite the fact that the detected winged cusp is not physiological, it still constitutes an organizing center for the model dynamics.

4.2 A physiological winged cusp universal unfolding in Hodgkin-Huxley model augmented with a slow regenerative ion channel

The missing element in Hodgkin-Huxley model to make the winged cusp physiological is a slow regenerative ion channel. Following [17], we add the calcium current

$$I_{Ca,L} = -\bar{g}_{Ca} d^a (V - V_{Ca}) \tag{14a}$$

$$\tau_d(V)\dot{d} = -d + d_\infty(V - V_{1/2,Ca}) \tag{14b}$$

in this model. Calcium activation provides positive feedback in the slow time scale of potassium activation. Picking the maximal conductance $\bar{g}_{Ca}$ as the bifurcation parameter and $(I, \bar{g}_{Na}, V_{1/2,Ca})$ as unfolding parameters, we now find a winged cusp at

$$V = V^\star \simeq -5,\ \bar{g}_{Ca} = \bar{g}^\star_{Ca} \simeq 0.3,$$

$$I_{app} = I^\star_{app} \simeq -61,\ \bar{g}_{Na} = \bar{g}^\star_{Na} \simeq 830,\ V_{1/2,Ca} = V^\star_{1/2,Ca} \simeq -17,$$

which is in the physiological range of all variables and parameters. Its universal unfolding is illustrated in Fig. 10.

4.3 A general algorithm to trace the winged cusp

The winged cusp detection illustrated in the previous section can be generalized to arbitrary conductance-based models (12). The bifurcation parameter is the maximal conductance $\bar{g}_{bif}$ of a slowly (in)activated ion channel (for instance a calcium channel of type T). The unfolding parameters are chosen as the applied current I_{app}, the maximal conductance $\bar{g}_{unf}$ of an ion channel with a fast gating variable (usually, the transient sodium channel), and the half activation potential $V_{1/2}$ of one of the gating variable. Let

$$G(V, \bar{g}_{bif}, I_{app}, \bar{g}_{unf}, V_{1/2}) = 0 \tag{15}$$

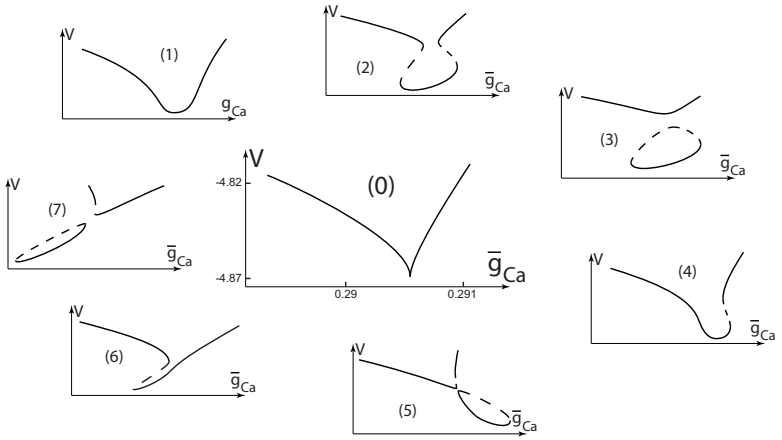

Figure 10: **Universal unfolding of the winged cusp singularity in the Hodgkin-Huxley model augmented with a slow regenerative current.** (0) Organizing center for $I_{app} = I^\star_{app},\ \bar{g}_{Na} = \bar{g}^\star_{Na},\ V_{1/2,Ca} = V^\star_{1/2,Ca}$ (see main text for approximate values). (1-7) Persistent bifurcation diagrams (cf. [2, Fig. IV.4.3]).

be the resulting fixed point equation associated to (12) and obtained by setting $x^f = x^f_\infty(V)$, $x^s = x^s_\infty(V)$, for all fast and slow gating variables, and $x^a = \bar{x}^a$, for all adaptation variables (12a), where $\bar{x}_a$ is in the physiological range of the associated variable. The following algorithm "detects" the universal unfolding of the winged cusp bifurcation in (12).

Algorithm (Universal unfolding of the winged cusp in conductance-based models)

A - Balance equation: by linearity in the unknown, analytically solve the balance equation

$$\sum_{x^s} \frac{\partial \dot{V}}{\partial x^s} \frac{\partial x^s_\infty}{\partial V} = 0.$$

in $\bar{g}_{bif}$.

B - Singularity condition: Plug the obtained solution $g_{bif,bal}(V, I_{app}, g_{unf})$ in the equation

$$\frac{\partial \dot{V}}{\partial V} + \sum_{x^f} \frac{\partial \dot{V}}{\partial x^f} \frac{\partial x^f_\infty}{\partial V} = 0.$$

and, again by linearity, solve the resulting equation analytically in $\bar{g}_{unf}$. Let $\bar{g}^*_{unf}(V, V_{1/2})$ be the obtained solution.

C - Degeneracy conditions 1: numerically solve the system of equations

$$\begin{cases} \dfrac{\partial^2 G}{\partial V^2}(V,\ \bar{g}_{bif,bal}(V, \bar{g}^*_{unf}(V, V_{1/2}), V_{1/2}),\ \bar{g}^*_{unf}(V, V_{1/2}),\ V_{1/2,Ca}) = 0 \\ \dfrac{\partial^2 G}{\partial \bar{g}_{bif} \partial V}(V,\ V_{1/2}) = 0 \end{cases}$$

in $(V, V_{1/2})$. Let $V^\star, V^\star_{1/2}$ be the obtained solution and define

$$\begin{aligned} \bar{g}^\star_{unf} &:= \bar{g}^*_{unf}(V^\star, V^\star_{1/2}) \\ \bar{g}^\star_{bif} &:= \bar{g}_{bif,bal}(V^\star, \bar{g}^\star_{unf}, V^\star_{1/2}) \\ I^\star_{app} &= -G(V^\star, \bar{g}^\star_{bif}, 0, \bar{g}^\star_{unf}, V^\star_{1/2}). \end{aligned}$$

D - *Degeneracy conditions 2*: Let

$$\tilde{\bar{g}}_{bif} = \bar{g}_{bif}, \quad \tilde{I}_{app} = I_{app} - \frac{\partial G}{\partial \lambda}(V^\star, V^\star_{1/2})(\bar{g}_{bif} - \bar{g}^\star_{bif}) - (\bar{g}_{bif} - \bar{g}^\star_{bif})^2, \tag{16}$$

and define

$$\tilde{G}(V, \bar{g}_{bif}, I_{app}, \bar{g}_{unf}, V_{1/2}) := G(V, \tilde{\bar{g}}_{bif}, \tilde{I}_{app}, \bar{g}_{unf}, V_{1/2}).$$

Note that, by construction

$$\tilde{G} = \frac{\partial \tilde{G}}{\partial V} = \frac{\tilde{\partial} G}{\partial \bar{g}_{bif}} = \frac{\partial^2 \tilde{G}}{\partial V^2} = \frac{\partial^2 \tilde{G}}{\partial V \partial \bar{g}_{bif}} = 0,$$

at $(V^\star, \bar{g}^\star_{bif}, I^\star_{app}, \bar{g}^\star_{unf}, V^\star_{1/2})$. Then, we have the following claim, which can numerically be proved in specific conductance-based models by applying the above algorithm and by verifying the different non degeneracy conditions in [2, Propositions II.9.4 and III.4.5]. Such conditions will generically be verified in the model parameter space.

Claim 1 *For a conductance-based model (12), generically in the model parameters, the bifurcation problem*

$$\tilde{G}(V, \bar{g}_{bif}, I^\star_{app}, \bar{g}^\star_{unf}, V^\star_{1/2}) = 0$$

is strongly equivalent (in the sense of [2]) to the winged cusp in a neighborhood of $(V^\star, \bar{g}^\star_{bif})$ *and, moreover, the three parameter unfolding*

$$\tilde{G}(V, \bar{g}_{bif};\ I_{app}, \bar{g}_{unf}, V_{1/2}) = 0$$

is its universal unfolding.

5 Why the winged cusp?

The analysis in this paper suggests that any conductance-based model that possesses a regenerative ionic current in addition to the two currents of Hodgkin-Huxley model is likely to contain a winged cusp singularity in a physiologically plausible range of parameters. This winged cusp organizes a three-time scale burster through the slow variation of the bifurcation parameter (a balance between restorative and regenerative slow channels) and the ultra-slow variation of an affine unfolding parameter (ultra-slow adaptation current). This result has both mathematical and physiological relevance.

Mathematically, the proposed approach selects one out of many possible bursting attractors for the mathematical modeling of neuronal bursting. There is a rich history of mathematical modeling of bursting, including several efforts to classify bursters mathematically and physiologically, see [18, 19, 20] and the list of references in [11, page 187]. Izhikevih distinguishes among 16 different bursters according to the two bifurcations that determine the resting-spike bistable range of the model when freezing the ultra-slow variable. Our three time-scales burster is of saddle-homoclinic type because both the saddle and the homoclinic bifurcation emerge together from a transcritical bifurcation in the universal unfolding of the winged cusp (Figure 2). The unstable nature of the homoclinic orbit near the singular limit selects the "fold/fold cycle" subtype for sufficiently small ε, but also in that type the key element is the homoclinic bifurcation generating the unstable limit cycle. For larger ε the homoclinic orbit becomes stable, but the underlying geometric structure does not change. It should be emphasized that this single geometric attractor accounts for different bursting wave forms. Figure 11 illustrates three bursting traces that can be reproduced with model (11). Parameters differ but the geometric attractor is the same. This is in contrast with the distinct mathematical models that have been proposed

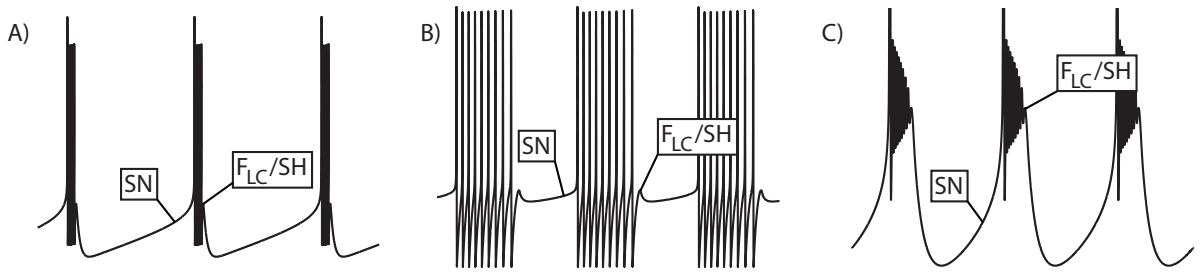

Figure 11: **Different bursting wave forms in model (11) share the same geometric attractor. A.** "Square-wave" bursting. **B.** "Parabolic" bursting. **C.** Square-wave with small amplitude action potentials (spikelets). SN: saddle-node bifurcation. F_{LC}: fold limit cycle bifurcation. SH: saddle-homoclinic bifurcation. Parameter values are provided in Section C.

in the literature to describe parabolic bursting [21] and square-wave bursting with both large [22, 23] and small [24, Fig. 9C] amplitude action potentials.

The bursting attractor of Theorem 3 is fundamentally associated to regenerative excitability of its slow-fast subsystem (region IV in Fig. 8). The discussion in [4] shows that the bistable range of regenerative excitability is, in first approximation, independent on the time-scale separation between the fast and slow variable. This is in sharp contrast with the bistable range of restorative excitability, which necessarily vanish in slow-fast models. For this reason, bursting models associated to restorative excitability (such as elliptic bursting [7]) have less modeling relevance in the particular context of endogenous neuronal bursting.

In addition to broad regions of restorative and regenerative excitability, Fig. 8A shows a small parametric region of mixed excitability (type V in the terminology of [3]). Like regenerative phase portraits, phase portraits in this region have a persistent bistable range, but it is of fold/ fold type, with a down-state that is a regenerative fixed point and a up-state that is either a restorative fixed point or a limit cycle (emerging from a hopf bifurcation within or outside the bistable range). The bursting attractor observed in this region can be considered as a variant of the bursting attractor associated to regenerative excitability. Both bursting attractors share the same geometry of hysteretic paths in the unfolding of the winged cusp singularity but the fold/fold variant exhibits the peculiar wave form illustrated in Fig. 12, usually studied under the name of "tapered" bursting in the literature, see e.g. [11].

It is remarkable that the four different waves shown in Fig. 11 and Fig. 12 can be modeled by the same geometric attractor. A companion paper in preparation further investigates the physiological mechanisms that determine the wave shape of the bursters, suggesting that two parameters are sufficient to determine the bursting wave within the unfolding of the winged cusp singularity.

The strong agreement between the mathematical insight provided by singularity theory and the known electrophysiology of bursting is another attractive feature of the proposed approach. There is a direct correspondence between the bifurcation and unfolding parameters of the winged cusp and the physiological minimal ingredients of a neuronal burster. In particular, our analysis predicts that any bursting neuron must possess at least one physiologically regulated regenerative channel. This prediction needs to be tested systematically but we have found no counter-example in the bursting neurons we have analyzed to date.

In spite of the vast diversity of ion channels encountered in different neurons and the resulting vast diversity of regulation mechanisms of bursting signaling, singularity theory suggests an apparent simplicity and universality in the organizing center of neuronal bursters. Such an insight is perhaps a central role of mathematical modeling.

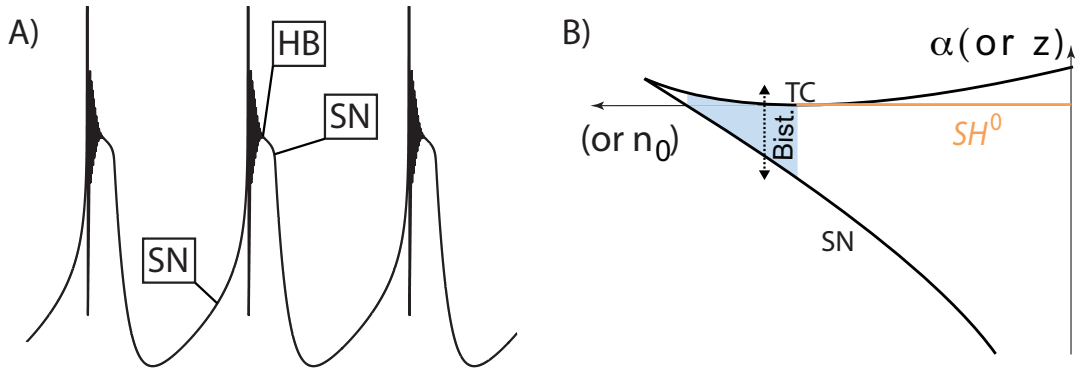

Figure 12: **Variant of the saddle-homoclinic bursting attractor in model (11). A.** When the fast-slow subsystem (11a-11b) exhibits Type V excitability [3], the bistable range is of fold / fold type leading to a "tapered" bursting waveform. Parameters values are provided in Section C. **B.** The hysteretic path associated to this type appears along path *ii)* of Fig. 8. Both its the up and down attractors lose stability in a saddle-node bifurcation. Depending on the excitability subtype, the burst onset can either exhibit damped spiking oscillations ending in a Hopf bifurcation within the bistable range (a situation captured by the bifurcation diagram in [3, Fig. 5.2]) or a single action potential (a situation captured by the bifurcation diagram in [3, Fig. 5.3]).

6 Conclusion

The paper proposes a three-time scale bursting theory rooted in singularity theory. The connection exploits both the three time-scale nature of experimentally recorded neuronal bursters and the peculiar feature of conductance based models to capture the equilibrium structure in a single scalar-valued algebraic equation. In this way, the global geometry of a non trivial dynamical attractor is reduced to a local algebraic analysis. The construction is general and the use of a local analysis tool to unfold the global geometry of singularly perturbed attractors seems of independent interest.

Even though the proposed three-time scale bursting model derives from a purely mathematical construction, it has an attractive neurophysiological interpretability. Singularity theory suggests that the route to bursting is organized by few parameters that have direct physiological interpretation and relevance. We are not aware of an earlier mathematical model of bursting that provides a physiologically meaningful route from tonic spiking to bursting. Furthermore, the proposed algorithmic procedure to trace a winged cusp singularity in arbitrary conductance based-models provides a simple method to extract few key parameters (such as the bifurcation parameter, the unfolding parameter, and the relative time-scale separation) from high-dimensional physiological models containing many unknown parameters. Those features are appealing to address system questions such as sensitivity, robustness, and homeostasis issues.

7 Acknowledgments

Prof. M. Golubitsky is gratefully acknowledged for insightful comments and suggestions during the visit of the first author at the Mathematical Bioscience Institute (Ohio State University).

A Codimension 1 and 2 bifurcation varieties in (7)

The fixed point equation of (7) is organized by a winged cusp at $x_{wcusp} := \frac{1}{3}$, $\lambda_{wcusp} := 0$, $\alpha_{wcusp} := -\frac{1}{27}$, $\beta_{wcusp} := -\frac{1}{3}$, $\gamma_{wcusp} := -2$. Codimension 1 transcritical and hysteresis bifurcation transition varieties in its unfolding are defined by

$$\alpha_{TC}(\beta,\gamma) = -\bar{x}_{TC}^3 - (\bar{\lambda}_{TC} + \bar{x}_{TC})^2 + \beta\bar{x}_{TC} - \gamma\bar{x}_{TC}(\bar{\lambda}_{TC} + \bar{x}_{TC}) \tag{17}$$

with

$$\bar{x}_{TC}(\beta,\gamma) = \frac{\gamma^2 - (\gamma^4 + 48\beta)^{1/2}}{12} \tag{18a}$$

$$\bar{\lambda}_{TC}(\beta,\gamma) = -\frac{\bar{x}_{TC}(2+\gamma)}{2} \tag{18b}$$

and

$$\alpha_{HY}(\beta,\gamma) = -\bar{x}_{HY}^3 - (\bar{\lambda}_{HY} + \bar{x}_{HY})^2 + \beta\bar{x}_{HY} - \gamma\bar{x}_{HY}(\bar{\lambda}_{HY} + \bar{x}_{HY}) \tag{19}$$

with

$$\bar{x}_{HY}(\gamma) = -\frac{1+\gamma}{3} \tag{20a}$$

$$\bar{\lambda}_{HY}(\beta,\gamma) = \frac{\beta - 3\bar{x}_{HY}^2 - \bar{x}_{HY}(2+2\gamma)}{2+\gamma} \tag{20b}$$

respectively.

The codimension 2 pitchfork variety is defined by

$$\gamma_{PF}(\beta) = \left(3\beta + \left(9\beta^2 + \frac{1}{27}\right)^{1/2}\right)^{1/3} - \frac{1}{\left(3\beta + \left(9\beta^2 + \frac{1}{27}\right)^{1/2}\right)^{1/3}} - 1 \tag{21a}$$

$$\alpha_{PF}(\beta) = -\bar{x}_{PF}^3 - (\bar{\lambda}_{PF} + \bar{x}_{PF})^2 + \beta\bar{x}_{PF} - \gamma\bar{x}_{PF}(\bar{\lambda}_{PF} + \bar{x}_{PF}) \tag{22}$$

with

$$\bar{x}_{PF}(\beta) = -\frac{1+\gamma_{PF}}{3} \tag{23a}$$

$$\bar{\lambda}_{PF}(\beta) = \frac{\beta - 3\bar{x}_{PF}^2 - \bar{x}_{PF}(2+2\gamma_{PF})}{2+\gamma_{PF}} \tag{23b}$$

B Proofs

B.1 Proof of Theorem 1

For $\lambda = 0$ and $\beta \in (0,1)$ there is only one nullcline intersection at the origin. For sufficiently small ε this intersection is unstable and the existence of a periodic orbit alternatively shadowing the upper and lower branch of the hysteresis bifurcation diagram follows along the same lines as [25]. □

B.2 Proof of Theorem 2

We rely on geometric singular perturbation arguments [26, 27, 25, 28, 29]. The reduced dynamics associated to (7), evolving on the slow time scale $\tau = \varepsilon t$, is given by

$$0 = G^s_{wcusp}(x, \lambda + y;\ \alpha, \beta, \gamma) \tag{24a}$$

$$\dot{y} = x - y, \tag{24b}$$

whereas the associated layer dynamics, evolving on the fast time scale t, is given by

$$\dot{x} = G^s_{wcusp}(x, \lambda + y;\ \alpha, \beta, \gamma) \tag{25a}$$
$$\dot{y} = 0. \tag{25b}$$

We construct the singular bistable phase portrait starting from the degenerate situation in Fig. 3 center, corresponding to a pitchfork bifurcation. The same qualitative phase portrait is obtained on the pitchfork variety (21) for all $\beta > \beta_{wcusp}$. Perturbing γ out of the pitchfork variety, but remaining on the transcritical variety defined by (17), the phase portrait perturbs to one of the two qualitative situations in Fig. 3 center - top or bottom. Finally, for λ below and sufficiently near $\lambda_{TC}(\beta, \gamma)$ and α below and sufficiently near $\alpha_{TC}(\beta, \gamma)$ one obtains the qualitative slow-fast dynamics in Fig. 13A, which leads to the singular phase-portrait in Fig. 13B. The following lemma summarizes this construction.

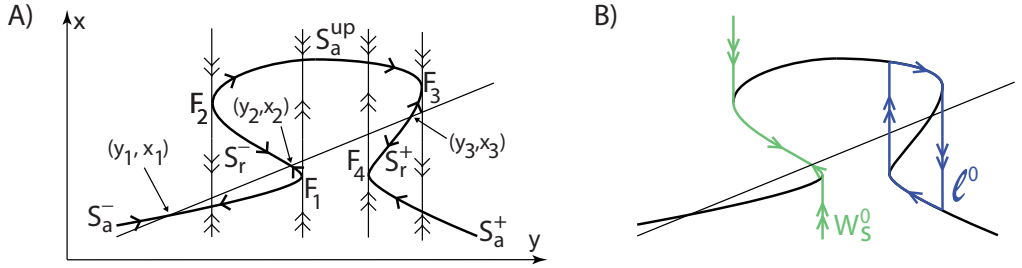

Figure 13: **Slow fast dynamics associated to (24-25).**

Lemma 1 *For all $\beta > \beta_{wcusp}$, there exists $\Delta_\gamma > 0$ such that, for all $\gamma \in (\gamma_{PF}(\beta) - \Delta_\gamma, \gamma_{PF}(\beta) + \Delta_\gamma)$, there exists $\Delta_\lambda > 0$ such that, for all $\lambda \in (\bar{\lambda}_{TC}(\beta, \gamma) - \Delta_\lambda, \bar{\lambda}_{TC}(\beta, \gamma))$, there exists $\Delta_\alpha > 0$ such that, for all $\alpha \in (\alpha_{TC}(\beta, \gamma) - \Delta_\alpha, \alpha_{TC}(\beta, \gamma))$, the following hold* (refer to Fig. 13 - left for the notation)*:*

- *i) The critical manifold of the slow-fast dynamics (24-25) has a mirrored hysteresis shape. In particular, it is composed of the attractive branches S_a^-, S_a^+, and S_a^{up}, the repelling branches S_r^- and S_r^+, and the four folds F_i, $i = 1, \ldots, 4$, connecting them.*
- *ii) There are exactly three nullcline intersection (y_i, x_i), $i = 1, \ldots, 3$, belonging to S_a^-, S_r^-, and S_r^+, respectively.*

A direct geometric inspection reveals the presence of a singular periodic orbit ℓ^0 and a singular saddle separatrix W_s^0. These objects persist for $\epsilon > 0$, as proved in the following lemma, which proves Theorem 2.

Lemma 2 *Let (y_i, x_i), $i = 1, \ldots, 3$ be defined as in the statement of Lemma 1 ii). For all $\lambda, \alpha, \beta, \gamma$ satisfying conditions of Lemma 1, there exists $\bar{\varepsilon}$ such that, for all $\varepsilon \in (0, \bar{\varepsilon})$*

i) (y_1, x_1) is locally exponentially stable, (y_2, x_2) is a hyperbolic saddle, and (y_3, x_3) is locally exponentially unstable.

ii) There exists an exponentially stable relaxation oscillation limit cycle ℓ^ε surrounding (y_3, x_3).

iii) The stable manifold W_s^ε of (y_2, x_2) separates the basin of attraction of (y_1, x_1) and ℓ^ε.

Proof of Lemma 2.

i) From Lemma 1, the fixed point (y_1, x_1) belongs to the attractive branch $\mathcal{S}_a^-$ of the critical manifold $\mathcal{S}$. Moreover, it is an exponentially stable fixed point of the the reduced dynamics (24). From the results in [26], there exists $\bar{\varepsilon}_1$ such that, for all $\epsilon \in (0, \bar{\varepsilon}_1]$, (y_1, x_1) is an exponentially stable fixed point of (7). The fixed point (y_2, x_2) belongs to

the repelling branch $\mathcal{S}_r^-$ of the critical manifold $\mathcal{S}$. Moreover, it is an exponentially stable fixed point of the reduced dynamics (24). Again from [26], there exists $\bar{\varepsilon}_2$ such that, for all $\epsilon \in (0, \bar{\varepsilon}_2]$, there exists an exponentially unstable local invariant manifold $W^{\varepsilon}_{s,loc}$ such that all trajectories starting in $W^{\varepsilon}_{s,loc}$ approach (y_2, x_2) exponentially fast. $W^{\varepsilon}_{s,loc}$ is the local stable manifold of (y_2, x_2). Its unstable manifold is given by the fiber of the unstable manifold of $W^{\varepsilon}_{s,loc}$ passing through (y_2, x_2). The fixed point (y_3, x_3) belong to the repelling branch $\mathcal{S}_r^+$ of the critical manifold $\mathcal{S}$, moreover it is an exponentially unstable fixed point of the reduced dynamics (24). By [26], there exists $\bar{\varepsilon}_3 > 0$ such that, for all $\epsilon \in (0, \bar{\varepsilon}_3]$, (y_3, x_3) is an exponentially unstable fixed point of (7).

ii) The slow fast dynamics possesses a singular periodic orbit ℓ^0 (See Fig. 13). Following [25], there exists $\bar{\varepsilon}_4$ such that, for all $\epsilon \in (0, \bar{\varepsilon}_4]$, there exists an exponentially stable relaxation oscillation limit cycle ℓ^{ε} surrounding (y_3, x_3).

iii) In backward time, trajectories of the reduced dynamics (24) starting on $\mathcal{S}_r^-$ in a neighborhood of (y_2, x_2) approach either the fold $\mathcal{F}_1$ or the fold $\mathcal{F}_2$. Following [29], there exists $\bar{\varepsilon}_5$ such that, for all $\epsilon \in (0, \bar{\varepsilon}_5]$, all trajectories starting in the local stable manifold $W^{\varepsilon}_{s,loc}$ approach (in backward time) either the fold $\mathcal{F}_1$ or the fold $\mathcal{F}_2$ along an invariant manifold W^{ϵ}_s, which continues after the fold singularities roughly parallel to trajectories of the layer problem. Therefore, the branch that continues after $\mathcal{F}_1$ extends to $x = -\infty$, whereas the branch that continues after $\mathcal{F}_2$ extends to $x = +\infty$. The invariant manifold W^{ϵ}_s is the saddle stable manifold and separates the plane in two disconnected regions that contain, respectively, the two attractors (y_1, x_1) and ℓ^{ε}.

Items *i)*, *ii)*, and *iii)* are proved by picking $\bar{\varepsilon} = \min_{i=1,\dots,5} \bar{\varepsilon}_i$. □

□

B.3 Proof of Theorem 3

Starting from a set of parameter satisfying the condition of Lemma 1 and increasing α to $\alpha = \alpha_{TC}(\beta, \gamma)$ the two folds F_1 and F_4 in Fig. 13A approach each other and eventually collide in a transcritical singularity TC, as in the slow-fast dynamics in Figure 14A. A direct geometrical inspection reveals the presence of a singular saddle-homoclinic trajectory SH^0 (Fig. 14B) for which the transcritical singularity serves as connecting point. This homoclinic orbit persists for $\varepsilon > 0$, as sketched in Figure 15A. On the contrary, decreasing α the two folds move away from each other until the left branch of the mirrored hysteresis is tangent to the y nullcline at a saddle-node bifurcation SN and eventually remains on its left, as in Fig. 15B. The following lemma summarizes this analysis. For its statement, we refer to Figures 13 and 14.

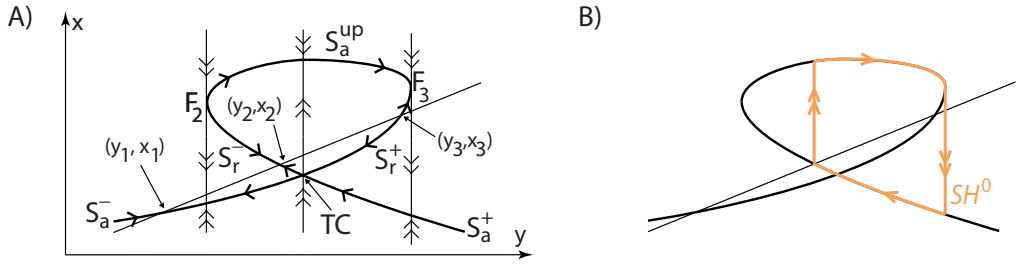

Figure 14: **Slow fast dynamics associated to (24-25).**

Lemma 3 *For all $\beta > \beta_{wcusp}$, there exists $\Delta_\gamma > 0$ such that, for all $\gamma \in (\gamma_{PF}(\beta) - \Delta_\gamma, \gamma_{PF}(\beta) + \Delta_\gamma)$, there exist $\Delta_\lambda > 0$ such that, for all $\lambda \in (\bar{\lambda}_{TC}(\beta, \gamma) - \Delta_\lambda, \bar{\lambda}_{TC}(\beta, \gamma))$ the following hold:*

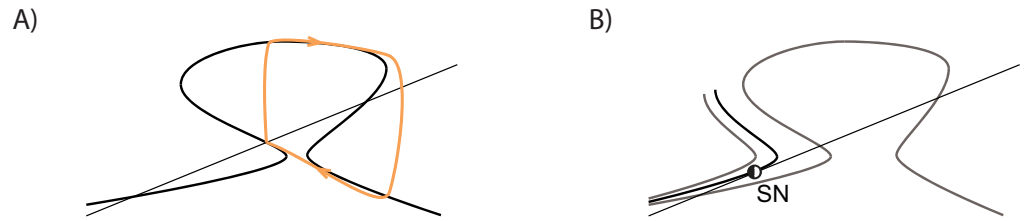

Figure 15: **Phase portrait of (7), with parameters and the function y_∞ satisfying conditions of Lemma 3**. **A.** Singularly perturbed saddle-homoclinic trajectory for $\alpha = \alpha^0_{SH} + \alpha_c(\sqrt{\varepsilon})$. **B.** Saddle-node bifurcation.

i) Let $\alpha^0_{SH} := \alpha_{TC}(\beta,\gamma)$. There exists $\bar\varepsilon > 0$ and a smooth function $\alpha_c(\cdot)$ defined on $\left[0,\sqrt{\bar\varepsilon}\right]$, and satisfying $\alpha_c(0) = 0$ and $\alpha_c(\sqrt{\varepsilon}) < 0$, for all $\varepsilon \in (0,\bar\varepsilon]$, such that, for $\alpha = \alpha^\varepsilon_{SH} := \alpha^0_{SH} + \alpha_c(\sqrt{\varepsilon})$, (7) has an unstable saddle-homoclinic orbit SH^ε.

ii) For all $\varepsilon > 0$, there exists $\alpha_{SN} < \alpha^0_{SH}$ such that (7) has a non-degenerate saddle-node bifurcation for $\alpha = \alpha_{SN}$ at which the node (y_1,x_1) and the saddle (y_2,x_2) merge.

iii) For all $\alpha \in [\alpha_{SN},\alpha^0_{SH})$ the nullcline intersection (y_3,x_3) belongs to the repelling branch S^+_r (where S^+_r is defined as in Figure 13A).

Proof of Lemma 3. *i)* For γ in a neighborhood of $\gamma_{PF}(\beta)$, $\alpha = \alpha_{TC}(\beta,\gamma)$ and λ smaller than and sufficiently near to $\bar\lambda_{TC}(\beta,\gamma)$, there are exactly three nullcline intersections (y_i,x_i), $i = 1,2,3$, belonging to the attractive branch S^-_a, the repelling branch S^-_r, and the repelling branch S^+_r, respectively. Then, the existence part of *i)* relies on the result in [28] and follows exactly the same step as in [3, Section 6.1]. It is therefore omitted. The resulting saddle-homoclinic trajectory is sketched in Fig. 15A. To prove that such homoclinic trajectory is unstable, recall that the stability of a saddle-homoclinic orbit is determined by the saddle quantity σ, that is, the trace of the Jacobian computed at the saddle and at the saddle-homoclinic bifurcation: if $\sigma > 0$ (resp. $\sigma < 0$) the homoclinic orbit is unstable (resp. stable). The Jacobian J_{SH} of (7) computed at (y_2,x_2) at the saddle-homoclinic bifurcation has the form

$$J_{SH} = \begin{pmatrix} a & b \\ \varepsilon c & -\varepsilon d \end{pmatrix}, \quad a,d > 0,\ b,c \in \mathbb{R}.$$

Therefore the saddle quantity $\sigma = a - \varepsilon d > 0$, for all $0 < \varepsilon < a/d$.

ii) For γ in a neighborhood of $\gamma_{PF}(\beta)$, $\alpha = \alpha_{TC}(\beta,\gamma)$, and λ smaller than and sufficiently near to $\bar\lambda_{TC}(\beta,\gamma)$, the (cubic) fixed point equation $G_{wcusp}(x,\lambda+x;\alpha,\beta,\gamma)$ has three roots, corresponding to the three fixed point (y_i,x_i), $i = 1,2,3$ of point *i)*. Decreasing α, the two smaller roots (corresponding to the fixed point (y_1,x_1) and (y_2,x_2)) approach each other and eventually merge in a quadratic zero for $\alpha = \alpha_{SN}$ corresponding to a non-degenerate saddle-node bifurcation.

iii) We prove the statement for $\gamma = \gamma_{PF}(\beta)$ since, by continuity, the same will hold in a neighborhood. When $\gamma = \gamma_{PF}(\beta)$, $\alpha = \alpha_{PF}(\beta)$, and λ is smaller than and sufficiently near to $\bar\lambda_{PF}(\beta)$, the nullcline intersection (y_3,x_3) lies on S^+_r. By continuity, the same is true for all α close to $\alpha_{PF}(\beta)$. Since the value $\alpha_{SN} \uparrow \alpha_{PF}(\beta)$ continuously as $\lambda \uparrow \bar\lambda_{PF}(\beta)$, one can pick λ sufficiently close to $\bar\lambda_{PF}(\beta)$ such that (y_3,x_3) lies on S^+_r for all $\alpha \in [\alpha_{SN},\alpha_{PF}(\beta))$. □

Lemmas 2 and 3 imply that there exists $\bar\varepsilon$ such that, for all $\varepsilon \in (0,\bar\varepsilon]$ and parameters satisfying condition of Lemma 3, the qualitative bifurcation diagram of (9a-9b) with respect to z is as in Figure 16. The fold limit cycle bifurcation for α_{FLC} arises from the fact that the saddle-homoclinic bifurcation is unstable near the singular limit. Hence, the stable branch of stable periodic orbits P^ε can not end at this bifurcation. Since the only

other bifurcation of planar limit cycles not involving a Hopf point is the fold limit cycle bifurcation, the qualitative bifurcation diagram in Fig. 16 follows.

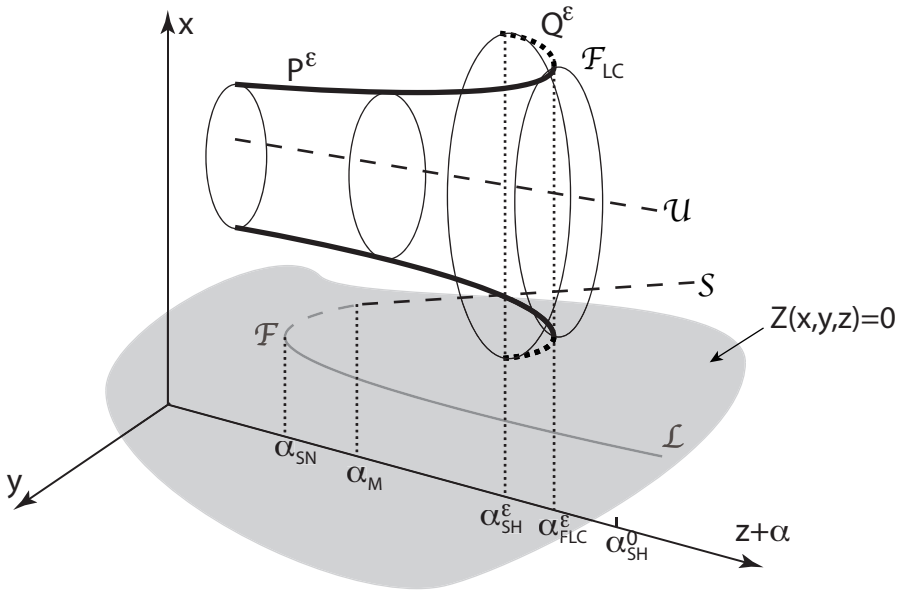

Figure 16: **Bifurcation diagram of (9a-9b) with respect to z and parameters satisfying condition of Lemma 3**. See the main text describing Fig. 5 for the notation.

We now follow [6, 7] to derive suitable conditions on Z such that z hysteretically modulates (9a-9b) along its rest spike bistable range. We pick Z such that the set $\{(x, y, z) \in \mathbb{R}^3 : \ Z(x, y, z) = 0\}$ can be expressed as the graph $\{x = h(y, z)\}$ and that it intersects the set of steady states and periodic and homoclinic orbits of the slow-fast subsystem (9a-9 only in one point belonging to the branch $\mathcal{S}$ of saddle points for $z + \alpha = \alpha_M \in (\alpha_{SN}, \alpha_{FLC})$, as in Figure 16. We also impose that for $x < h(y, z)$ the ultra-slow variable decreases, that is, $Z(x, y, z) < 0$, and vice-versa. Under these conditions on Z, Theorem 3 follows along the same line as the proofs in [6] (for the analysis near the branch of the stable steady states and the "jump up" at the fold bifurcation) and [7] (for the analysis near the branch of periodic orbits and the "jump down" at the fold limit cycle bifurcation). □

C Parameter for numerical simulations in Figs. 6, 7, 11, 12

For the sake of an easy numerical implementation and the reproduction of "nice" temporal traces, we suggest the following piecewise linear approximation of (11)

$$\dot{V} = kV - \frac{V^3}{3} - (n + n_0)^2 + I - z \tag{26a}$$

$$\dot{n} = \varepsilon_n \left(\hat{n}_\infty(V - V_0) - n\right) \tag{26b}$$

$$\dot{z} = \varepsilon_z(\hat{z}_\infty(V - V_1) - z) \tag{26c}$$

where

$$\hat{n}_\infty(V - V_0) := \begin{cases} k^n_-(V - V_0) & \text{if } V < V_0, \\ k^n_+(V - V_0) & \text{if } V \geq V_0. \end{cases}$$

with $0 \le k_-^n < 1$ and $k_+^n > 1$, and

$$\hat{z}_\infty(V - V_1) := \begin{cases} k_-^z(V - V_1) & \text{if } V < V_1, \\ k_+^z(V - V_1) & \text{if } V \ge V_1. \end{cases}$$

with $0 \le k_-^z < 1$ and $k_+^z > 1$.

Parameters used in Figs. 6 and 7 are $k = 1$, $I = 11/3$, $\varepsilon_n = 0.02$, $\varepsilon_z = 0.0005$, $V_0 = -0.5$, $k_-^n = 0.4$, $k_+^n = 7$, $V_1 = -1$, $k_-^z = 0$, $k_+^z = 50$. The bifurcation parameter is $n_0 = 0.3$ in Figure 6 left and $n_0 = -1.1$ in Fig. 6 right. In Fig. 7 n_0 is linearly (in time) decreased from 0.3 to -1.1.

Parameters used in Figs. 11A are $n_0 = -1.1$, $k = 1$, $I = 11/3$, $\varepsilon_n = 0.02$, $\varepsilon_z = 0.0005$, $V_0 = -0.5$, $k_-^n = 0.4$, $k_+^n = 7$, $V_1 = -1$, $k_-^z = 0$, $k_+^z = 50$.

Parameters used in Figs. 11B are $n_0 = -0.2$, $k = 1$, $I = 11/3$, $\varepsilon_n = 0.02$, $\varepsilon_z = 0.0002$, $V_0 = -0.5$, $k_-^n = 0.05$, $k_+^n = 7$, $V_1 = -0.5$, $k_-^z = 0$, $k_+^z = 50$.

Parameters used in Figs. 11C are $n_0 = -0.2$, $k = 0.12$, $I = 11/3$, $\varepsilon_n = 0.02$, $\varepsilon_z = 0.001$, $V_0 = -0.5$, $k_-^n = 0.4$, $k_+^n = 7$, $V_1 = -0.5$, $k_-^z = 0$, $k_+^z = 50$.

Parameters used in Figs. 12A are $n_0 = -0.2$, $k = 0.7$, $I = 11/3$, $\varepsilon_n = 0.02$, $\varepsilon_z = 0.001$, $V_0 = -1.25$, $k_-^n = 0.9$, $k_+^n = 7$, $V_1 = -1.2$, $k_-^z = 0$, $k_+^z = 50$.

D Parameter for numerical simulations of the Hodgkin-Huxley model in Section 4.1

All the parameter and activation and inactivation rates are taken from the original paper [1]. The time constants $\tau_x(V)$ and steady state functions $x_\infty(V)$ are related to the activation and inactivation rates $\alpha_x(V)$ and $\beta_x(V)$, $x = m, n, h$, as follows

$$\tau_x(V) = \frac{1}{\alpha_x(V) + \beta_x(V)}, \quad x_\infty(V) = \frac{\alpha_x(V)}{\alpha_x(V) + \beta_x(V)}.$$

In accordance with the original paper [1], the potassium half-activation $V_{1/2,K} = 10mV$.

References

[1] A. Hodgkin and A. Huxley. A quantitative description of membrane current and its application to conduction and excitation in nerve. *J. Physiol*, 117:500–544, 1952.

[2] Martin Golubitsky and David G Schaeffer. Singularities and groups in bifurcation theory. volume i. 1985.

[3] A. Franci, G. Drion, and R. Sepulchre. An organizing center in a planar model of neuronal excitability. *SIAM J Appl Dyn Syst*, 11(4):1698–1722, 2012.

[4] A. Franci, G. Drion, V. Seutin, and R. Sepulchre. A balance equation determines a switch in neuronal excitability. *PLoS Comput Biol*, 9(5):e1003040, 2013.

[5] R. FitzHugh. Impulses and physiological states in theoretical models of nerve membrane. *Biophysical J*, 1:445–466, 1961.

[6] David Terman. Chaotic spikes arising from a model of bursting in excitable membranes. *SIAM Journal on Applied Mathematics*, 51(5):1418–1450, 1991.

[7] Jianzhong Su, Jonathan Rubin, and David Terman. Effects of noise on elliptic bursters. *Nonlinearity*, 17(1):133, 2004.

[8] R. Krahe and F. Gabbiani. Burst firing in sensory systems. *Nature Reviews Neuroscience*, 5(1):13–23, 2004.

[9] S. Astori, R. D. Wimmer, H. M Prosser, C. Corti, M. Corsi, N. Liaudet, A. Volterra, P. Franken, J. P. Adelman, and A. Lüthi. The CaV3. 3 calcium channel is the major sleep spindle pacemaker in thalamus. *Proceedings of the National Academy of Sciences*, 108(33):13823–13828, 2011.

[10] I. Putzier, P. H. M. Kullmann, J. P. Horn, and E. S. Levitan. CaV1. 3 channel voltage dependence, not Ca2+ selectivity, drives pacemaker activity and amplifies bursts in nigral dopamine neurons. *The Journal of Neuroscience*, 29(49):15414–15419, 2009.

[11] E.M. Izhikevich. *Dynamical Systems in Neuroscience: The Geometry of Excitability and Bursting*. MIT Press, 2007.

[12] J.N. Guzman, J. Sánchez-Padilla, C.S. Chan, and D.J. Surmeier. Robust pacemaking in substantia nigra dopaminergic neurons. *J Neurosci*, 29(35):11011–11019, 2009.

[13] X.J. Zhan, C.L. Cox, J. Rinzel, and S.M. Sherman. Current clamp and modeling studies of low-threshold calcium spikes in cells of the cats lateral geniculate nucleus. *Journal of neurophysiology*, 81(5):2360–2373, 1999.

[14] S.M. Sherman. Tonic and burst firing: dual modes of thalamocortical relay. *Trends Neurosci*, 24(2):122–126, 2001.

[15] J-C. Viemari and J-M. Ramirez. Norepinephrine differentially modulates different types of respiratory pacemaker and nonpacemaker neurons. *Journal of neurophysiology*, 95(4):2070–2082, 2006.

[16] J. Rinzel. Excitation dynamics: insights from simplified membrane models. In *Federation proceedings*, volume 44, page 2944. Fed Proc, 1985.

[17] G. Drion, A. Franci, V. Seutin, and R. Sepulchre. A novel phase portrait for neuronal excitability. *PLoS ONE*, 7(8):e41806, 08 2012.

[18] J. Rinzel. A formal classification of bursting mechanisms in excitable systems. In *Mathematical topics in population biology, morphogenesis and neurosciences*, pages 267–281. Springer, 1987.

[19] R. Bertram, M. J. Butte, T. Kiemel, and A. Sherman. Topological and phenomenological classification of bursting oscillations. *Bulletin of mathematical biology*, 57(3):413–439, 1995.

[20] M. Golubitsky, K. Josic, and T. J. Kaper. An unfolding theory approach to bursting in fast-slow systems. *Global analysis of dynamical systems*, pages 277–308, 2001.

[21] J. Rinzel and Y.S. Lee. Dissection of a model for neuronal parabolic bursting. *J Math Biol*, 25(6):653–675, 1987.

[22] J. L. Hindmarsh and R. M. Rose. A model of neuronal bursting using three coupled first-order differential equations. In *Proc. Roy. Soc. Lond*, volume B 221, pages 87–102, 1984.

[23] J. Rinzel and G.B. Ermentrout. Analysis of neural excitability and oscillations. In *Methods in neuronal modeling*, pages 135–169. MIT Press, 1989.

[24] A. A. Prinz, C. P. Billimoria, and E. Marder. Alternative to hand-tuning conductance-based models: construction and analysis of databases of model neurons. *Journal of Neurophysiology*, 90(6):3998–4015, 2003.

[25] M. Krupa and P. Szmolyan. Relaxation oscillation and canard explosion. *J. Differential Equations*, 174(2):312–368, 2001.

[26] N. Fenichel. Geometric singular perturbation theory. *J. Diff. Eq.*, 31:53–98, 1979.

[27] C.K.R. Jones. Geometric singular perturbation theory. In *Dynamical systems. Springer Lecture Notes in Math. 1609*, pages 44–120, Berlin, 1995. Springer.

[28] M. Krupa and P. Szmolyan. Extending slow manifolds near transcritical and pitchfork singularities. *Nonlinearity*, 14:1473–1491, 2001.

[29] M. Krupa and P. Szmolyan. Extending geometrical singular perturbation theory to nonhyperbolic points - folds and canards points in two dimensions. *SIAM J. Math. Analysis*, 33(2):286–314, 2001.